Application of terahertz Gouy phase shift from curved surfaces for estimation of crop yield

John F. Federici,[1,*] Robert L. Wample,[2] David Rodriguez,[1] and Suman Mukherjee[1]

[1]Department of Physics, New Jersey Institute of Technology, Newark, New Jersey 07102, USA

[2]Department of Viticulture and Enology, California State University–Fresno, Fresno, California 93740, USA

*Corresponding author: federici@adm.njit.edu

Received 27 October 2008; revised 26 January 2009; accepted 10 February 2009;
posted 11 February 2009 (Doc. ID 103183); published 25 February 2009

The application of terahertz time-domain spectroscopy (THz-TDS) and imaging to differentiate flat and curved surfaces in reflection via the THz Gouy phase shift is demonstrated. For a THz-TDS system that is aligned for reflection from a flat surface, the presence of a curved surface displaces the image focal plane from the detector plane, resulting in a Gouy phase shift. The potential of utilizing this configuration for estimating the number and size of curved objects is discussed with particular emphasis on agriculture crop yield estimates. © 2009 Optical Society of America

OCIS codes: 110.6795, 120.0280, 280.1415.

1. Introduction

The potential of terahertz (THz) spectroscopy and imaging for nondestructive evaluation of materials such as semiconductors and condensed matter, liquids [1,2], pharmaceuticals [3], and explosives [4,5] is well documented. The key attribute of THz nondestructive evaluation is the ability of THz radiation to propagate through barrier materials such as paper, plastic, and other nonmetallic containers. As THz technology has developed over the past 20 years, THz spectroscopy and imaging has been applied to a wider variety of materials, including food [6] and agricultural products. Agriculture applications include measuring the moisture content in leaves [7,8], density inhomogeneities and structural details of wood [9,10], grain [11,12], and the presence of defects and voids in natural cork [13].

It is a well-known property that electromagnetic waves acquire an extra π rad phase shift upon passing through a focal point. This effect was first discovered by Gouy in 1890 using optical beams. Using the mathematical formalism for Gaussian beam propagation, the Gouy phase shift appears as an added axial phase shift to the propagating beam [14] given by

$$\psi(z) = \tan^{-1}\left(\frac{z}{Z_R}\right), \tag{1}$$

where $Z_R = \pi\omega_o^2/\lambda$, where λ is the wavelength of the radiation, ω_o is the spot size of the beam at the focus, and the phase shift is measured relative to the phase at the focal point ($z = 0$) of the beam. Within distances of several Z_R from the focal point, the axial phase shift varies rapidly.

In this paper, the application of terahertz time-domain spectroscopy (THz-TDS) and imaging to differentiate flat and curved surfaces in reflection via the THz Gouy phase shift is explored. For a THz-TDS system that is aligned for reflection from a flat surface, the presence of a curved surface displaces the image focal plane from the detector plane, resulting in a measurable Gouy phase shift. The potential of utilizing this configuration for estimating the number and size of curved objects is demonstrated with particular emphasis on agriculture crop yield estimates. As a model system, we focus on demonstrating that THz imaging could be used to differentiate individual grape berries from stems, branches, and

0003-6935/09/071382-07$15.00/0

leaves. Using a laboratory THz imaging system, we follow the development of grape clusters from the formation of flowers (May) through harvest (September). The differentiation, which results from a Gouy phase shift from the curved berry surface, occurs early in the growing season while there is little foliage on the grape vines and continues until harvest.

This paper is organized as follows: methods and materials are described in Section 2. The results and implications of the presented results are presented in Section 3. Adaptation of the work presented here for crop yield estimates is presented in Section 4. Concluding remarks are presented in Section 5.

2. Methods and Materials

Niagra grape samples are acquired from a single 12 year old vine grown in central New Jersey. Samples are collected in the early morning. A section of vine including clusters, leaves, and stems is cut. After the initial cutting, the sample is cut again with its end submerged in water to eliminate any air bubbles that may have formed in the stem during the initial cut. During transportation to the laboratory and imaging experiments, the sample's stem is kept immersed in water to prevent drying of the sample during experimentation. Imaging experiments are typically completed within 3 h of cutting.

The THz reflection images of flowers, berries, stems, and leaves are acquired with a T-Ray 2000 Spectroscopy and Imaging system (Picometrix, Inc). Details of the THz time-domain method may be found in Ref. [1]. The system has a bandwidth of roughly 0.1 to 2.5 THz, corresponding to a wavelength range of 0.12 to 3 mm. A pair of silicon lenses (7.62 cm focal length) focuses the THz radiation to a spot at which the sample is placed. The angle between the incoming and reflected THz radiation is roughly 35°. The imaging system consists of a pair of computer controlled linear translation stages (1 μm resolution). The THz images are acquired by recording the THz reflected pulse at each sample position. A reflected pulse from a gold mirror is used as a reference. THz images are formed by measuring the full time-domain waveform within an 80 ps time window. The waveforms presented are an average of 10 individual waveforms. The sample is mechanically scanned in two directions at the focal point of the THz to generate an image one pixel at a time. Typical step sizes are 100–500 μm. Roughly 1 h is required to image a 7 cm^2 area with a 300 μm step size.

Both the phase and amplitude of the THz radiation as a function of frequency are acquired through a Fourier transform of the time-domain data. The silicon lenses introduce a small secondary pulse (located at ~62 ps in Fig. 3, below) due to multiple reflections of the THz beam in the lenses. When the time-domain data are Fourier transformed to the frequency domain, the multiple reflections would appear as interference fringes in the THz spectra. The fringes have been removed from the THz spectral data.

3. Results and Discussion

The THz reflection image of a group of three berries is shown in Fig. 1. The THz image is generated by measuring the total THz reflected power in the 0.3–0.4 THz bandwidth at each pixel. Pixels corresponding to large THz reflection are colored white. Black corresponds to no THz reflection detected. The brightest portion of the berry results from a specular reflection of the THz radiation from that particular location on the berry into the THz detector. It is well known that the water content in the leaves attenuates THz radiation. However, grape leaves transmit roughly 25% of the THz power at 200 GHz. To illustrate the potential of imaging grape clusters through a thin canopy, Fig. 1(D) illustrates an image of a grape berry hidden behind a grape leaf.

In order to understand the differences in the THz reflection of berries, leaves, and stems, we examine the spectral shape of the reflectivity at various positions of the samples. Figure 2 shows the reflectance spectra of the three berries and the leaf and stem. All of the spectra are from locations on the samples that exhibit a relative maximum in the THz reflectivity. In Fig. 2, it is clear that while there is some variability in the spectral reflectance of the berries, the magnitude and spectral shape of the reflectance are consistent among the three berries. In comparing the berries to the leaves and stems, the magnitude of the *E*-field reflectance of all three is typically in the 15–25% range. While there are spectral differences among the three in the magnitude of the reflectance, experimentation with many samples suggests that there does not appear to be any consistent trend that would allow one to differentiate among the three purely based on the magnitude of the reflectance.

In examining the phase of the reflected THz radiation, berries can easily be distinguished from stems

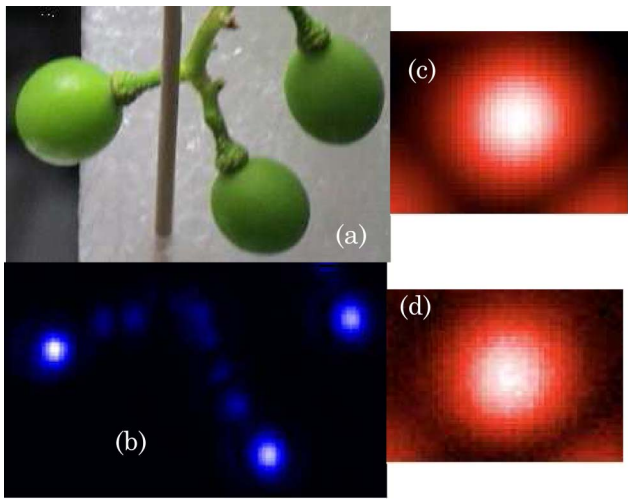

Fig. 1. (Color online) (A) Visible image of three grapes from 18 June. The toothpick in the picture is used to hold the sample fixed during the image acquisition. (B) Corresponding THz image. The image is 137 by 83 pixels. Each pixel is 0.3 mm square. THz images are based on average transmission between 0.15–0.2 THz of a grape (C) and a grape hidden behind a grape leaf (D).

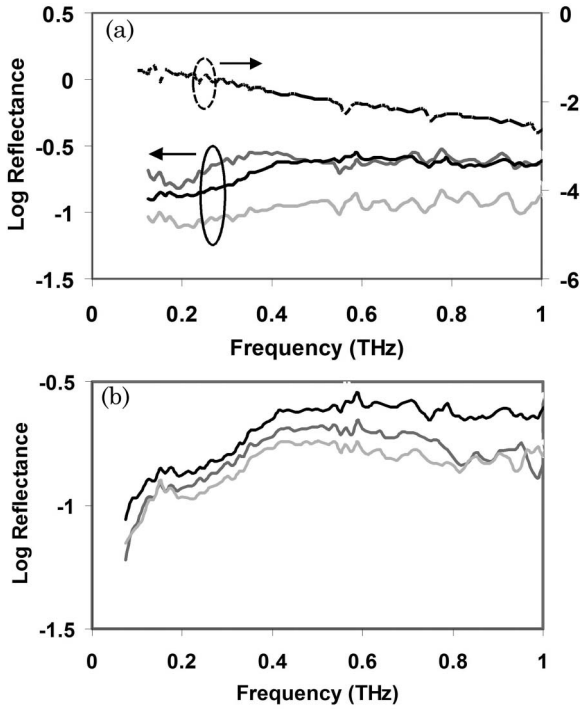

Fig. 2. (A) Comparison of the reflectance spectra (bottom three curves) of a berry (black), leaf (dark gray), and stem (light gray). The sharp peak near 0.557 THz is an artifact of absorption by ambient water vapor in the air. The spectra of the reference are shown in the dashed top curve. (B) Reflectance spectra of the three grapes (18 June) of Fig. 1. The interference fringes from multiple reflections in the silicon lenses have been removed. The signal THz signal from the berry is about 2 orders of magnitude above the noise floor of the THz system at 0.5 THz.

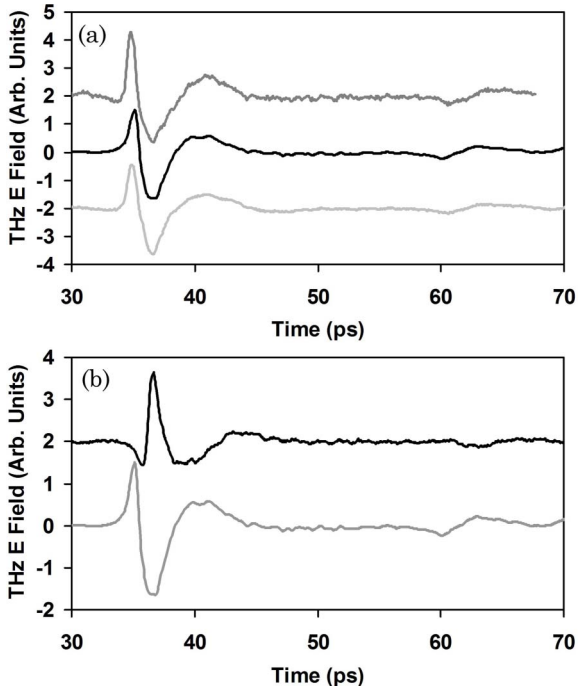

Fig. 3. (A) Comparison of THz time-domain waveforms (18 June) of the reference (middle trace), stem (upper), and leaf (lower) (B) reference (lower trace) and grape (upper trace). The time axes and amplitudes have been normalized for comparison of the pulse shapes. The traces are offset in the vertical direction for clarity. The reflection spectra of Fig. 2 are calculated from the magnitude of the Fourier transforms of the time-domain data. The small peaks in the data near 62 ps are from multiple reflections within the silicon lenses.

and leaves. Figure 3 shows a comparison between typical time-domain waveforms from a berry, leaf, stem, and reference flat gold mirror. Since the time location of the THz peak depends on the distance between the sample and the THz transmitters/receivers, we have shifted the time-domain waveforms in time and normalized their peak amplitudes to better compare their shape. In examining the time-domain waveforms of Fig. 3, clearly the berry's phase appears to be shifted with respect to the others. (Moreover, since the phase of the reflections from both the leaves and stems coincides with that from the reference mirror, a field system could use either of these reflections rather than a gold mirror as a reference.)

In determining the origin of the THz phase change upon reflection from the berries, tests were conducted to eliminate the possibility that details of the berry structure were responsible. If the skin of the berries was removed, similar THz waveforms and phase shifts were measured. Similar results have been obtained with a variety of thin-skinned, high-water-content fruit such as blueberries and cherries. Therefore, the properties of the THz reflection do not appear to be strongly dependent on the type of fruit that is imaged or on the details of the fruit's skin.

The phase change in THz reflection from berries can be explained by the Gouy effect [14,15]. An equivalent (transmission) optical system to our reflective experimental configuration is shown in Fig. 4, in which the berry is modeled as a diverging lens. The effective focal length of the diverging lens is related to the radius of curvature of the berry's surface by $f_g = R_g/2$. Referring to Fig. 4, in the absence of the berry (e.g., $R_g \to \infty$ so $f_g \to \infty$), the THz light is focused onto the THz receiver. For finite values of f_g, the THz radiation focuses at a point behind the detector location. Since the phase of the THz radiation varies significantly near a focal point according to the Gouy effect, the phase of the detected THz radiation will be altered substantially by the presence of the diverging lens. Figure 4(B) illustrates the change in the phase as a function of distance from the focal point of the light. In the plot, the distance Z_R is defined as $Z_R = \pi\omega_o^2/\lambda$, where λ is the wavelength of the radiation. Note that if the detector is located before the light comes to a focus, the phase shift approaches $-\pi/2$.

We determine the phase of the THz wave at the THz receiver (RX) using the ABCD matrix method [14,15] to propagate Gaussian beams through the optical configuration of Fig. 4(A). For this analysis we assume that the input beam at L2 is collimated (radius of curvature of the wave infinite) with a spot

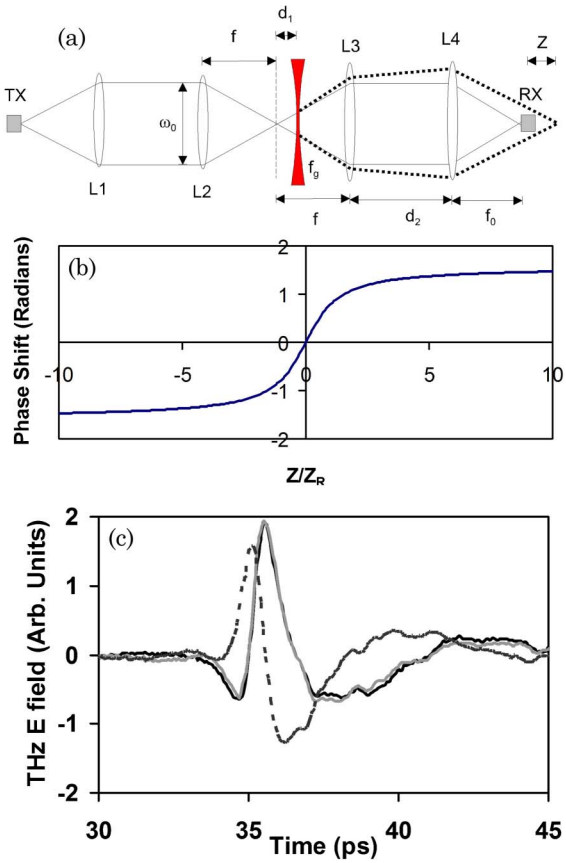

Fig. 4. (Color online) (A) For simplicity, the experimental reflective geometry is analyzed as a transmission system. The diverging lens (d_1) with focal length f_g in the figure represents the grape. THz radiation is emitted from the THz transmitter (TX) and collimated by lens L1 to a beam diameter of ω_0. Lens L2 (focal length f) focuses the THz radiation, while lens L3 (focal length f) collects the THz beam after focusing. In the absence of the diverging lens, lens L4 focuses the THz radiation on the THz receiver RX. When the diverging lens is present (dashed line), the THz radiation focuses at a point Z beyond the THz receiver. (B) Plot of Gouy phase shift as a function of distance Z. The optical configuration including the berry corresponds to a negative distance Z. (C) Measured reflected THz waveform from a typical grape (solid black curve). The dashed black curve corresponds to an added correction for the frequency dependent reflectivity of the berry but no correction to the phase shift. The addition of a $-\pi/2$ phase shift (gray curve) accurately reproduces the measured waveform.

size of ω_0. The propagation matrices to propagate a Gaussian beam from L2 to the THz receiver can be written as

$$\begin{bmatrix} A & B \\ C & D \end{bmatrix} = \begin{bmatrix} 1 & 0 \\ -1/f & 1 \end{bmatrix} \begin{bmatrix} 1 & f+d_1 \\ 0 & 1 \end{bmatrix} \begin{bmatrix} 1 & 0 \\ -1/f_g & 1 \end{bmatrix} \times \begin{bmatrix} 1 & f-d_1 \\ 0 & 1 \end{bmatrix} \begin{bmatrix} 1 & 0 \\ -1/f & 1 \end{bmatrix} \bullet \begin{bmatrix} 1 & d_2 \\ 0 & 1 \end{bmatrix} \times \begin{bmatrix} 1 & 0 \\ -1/f_o & 1 \end{bmatrix} \begin{bmatrix} 1 & f_o \\ 0 & 1 \end{bmatrix}. \quad (2)$$

The Gaussian beam parameters at the RX are given by

$$\hat{q}_{RX} = \frac{A\hat{q}_0 + B}{C\hat{q}_0 + D}, \quad (3)$$

where

$$\hat{q}_0 = i\frac{\pi\omega_o^2}{\lambda_0}; \quad (4)$$

λ_0 and ω_o are the vacuum THz wavelength and spot size of the Gaussian beam, respectively. The phase angle of the Gaussian beam at the RX may be written as

$$\exp(i\psi) = \frac{A + B/\hat{q}_0}{|A + B/\hat{q}_0|}. \quad (5)$$

In calculating the ABCD matrices, we make the assumption that the diverging lens (berry) is at the focus of the THz radiation so that $d_1 = 0$. Furthermore, we assume that the distance d_2 and focal length f_0 are chosen so that in the absence of the diverging lens, the THz radiation focuses on the THz RX.

Solving Eq. (2) for the case of $1/f_g = 0$ (i.e., no diverging lens present) gives $A = 0$ and $B = -f_0$, while for $1/f_g \neq 0$, $A = f^2/f_0 f_g$ and $B = -f_0$. The phase difference can be expressed using Eq. (5) as $\exp(i\psi_g - i\psi_0)$, where the subscripts g and 0 refer to the presence and absence of the berry, respectively. Using the values for A, B, and Eq. (5), the phase difference can be written as

$$\sin(\psi_g - \psi_0) = \frac{-f^2/f_o f_g}{[(f^2/f_o f_g)^2 + (\lambda_o f_o/\pi\omega_0^2)^2]^{1/2}}. \quad (6)$$

In estimating the phase shift for our experimental configuration, $f = f_0 = 7.6\,\text{cm}$, $f_g = 0.25\,\text{cm}$, and $\omega_0 = 4\,\text{cm}$, the first term in the denominator of Eq. (6) is much larger than the second. Consequently, the phase difference is essentially independent of the THz frequency with a value of $\psi_g - \psi_0 = -\pi/2$.

Figure 4(C) shows the measured reflected THz waveform from the berry of Fig. 3, as well as the predicted waveform based on Eq. (6). The predicted waveform is calculated from the reference waveform in which the berry is replaced by a flat gold mirror. We correct for the frequency dependent magnitude of the reflectance using the measured reflectivity (Fig. 2) for a berry. This correction includes not only the effect of the frequency dependent reflectance from the berry's surface but also changes in the measured THz amplitude due to the defocusing of the THz beam on the receiver. When the phase correction of Eq. (6) is included there is excellent agreement between the measured and predicted waveform.

Ideally, one would like an accurate estimation of the crop yield months before harvest. Clearly based on the phase information, grape berries can be differentiated from stems and leaves. However, is this true throughout the growing season? To answer this question, we have measured the THz reflection images

from stems, leaves, and grape clusters prior to bloom and after fruit set, from early May until late August. Figure 5(A) shows a visible image and THz time-domain waveforms from a flower cluster, stem, and leaf on 14 May. Unlike the time-domain pulses of Fig. 3 from berries, the relative phase of the reflected pulses from the flowers, stems, and leaves are essentially the same as the reference. In contrast, samples taken just two weeks later [Fig. 5(B)] behave quite differently with respect to the THz reflection. At this point in time, the grape cluster is postflowering but preshatter. All of the flowers/berries are still present. During development, the moisture content should be different in some of the berries. Some berries will not mature and consequently at a later time will fall off the cluster (shatter). The time-domain waveforms of Fig 5(B) show that the berries have begun to form. The figure shows the waveform from a berry of the inset in comparison to the reference reflection from a flat gold mirror. Clearly, the phase of the reflection from the berry is shifted by $-\pi/2$ rad relative to the reference. The phase of the reflections from the stems and leaves, however, maintains the same relative phase as the reference. Based on the THz phase measurements, THz imaging can differentiate between berries and stems/leaves very early in the growing season (1 June). In examining typical time-domain waveforms from grape clusters from 1 June through harvest, the general trend persists of a $-\pi/2$ phase shift from the berries relative to the reference. Time-domain waveforms from the stems/leaves also show a consistent trend of roughly maintaining the same phase relationship as the reference waveform.

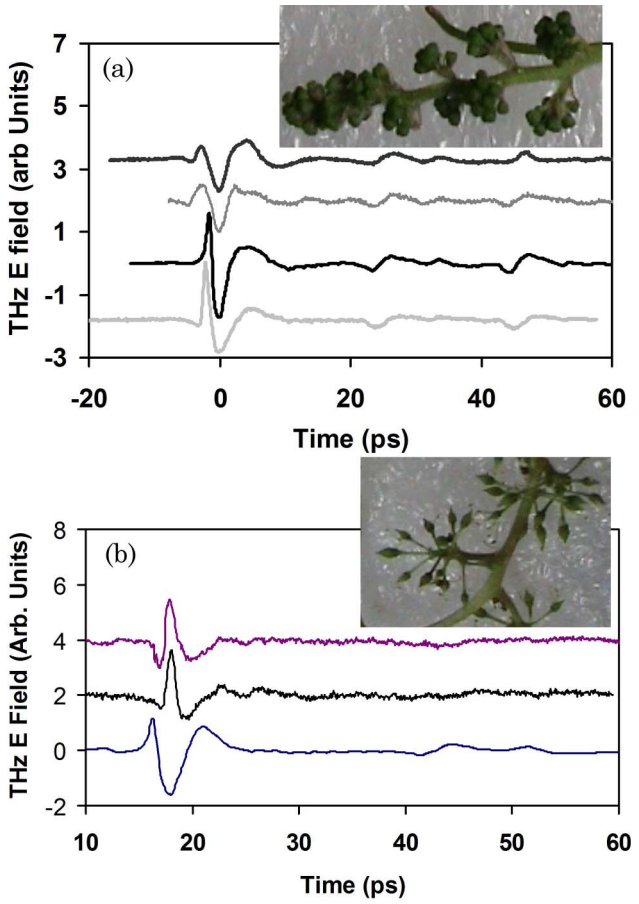

Fig. 5. (Color online) (A) Typical THz time-domain waveforms from bright reflection pixels of the leaf, flower, reference, and stem (from top curve to bottom). Inset: visible image of a flower cluster on 14 May prior to bloom. (B) Comparison among the reference waveform (bottom trace), the reflected THz waveform from a berry (1 June) in the inset (middle), and the predicted THz reflection (top) from the berry.

Estimation of grape yield includes three factors: clusters per vine, berries per cluster, and berry weight. As illustrated above, THz imaging can detect the presence of berries, enabling a measure of the number of clusters per vine. The number of berries per cluster can also be estimated. However, one has to account for "shadowing" effects as discussed in Section 4. Using THz imaging, we can possibly also estimate the berry weight, although our estimate will be indirect. In essence, we will measure the geometric size of the berry and infer the weight of the berry by knowing that there is a strong correlation between the berry's size and weight [16]. The size of the berry can be estimated by measuring the curvature of the berry's surface from the THz images (e.g., Fig. 1). The bright spots of Fig. 1 correspond to specular reflection from the berry's surface and an accompanying $-\pi/2$ rad phase shift. The reflection from any other location of the berry's surface is not specular. The tilt or inclination of the berry's surface at that point leads to the reflected pulse's following a slightly different path to the THz receiver. Consequently, the phase or shape of the detected THz pulse is distorted compared to the specular reflection from the berry.

Figure 6 shows the distortion of the THz pulse as one moves away from the peak of the specular reflection. The THz image of the top left berry in Fig. 1 is shown as an inset in Fig. 6. The specularly reflected THz pulse from the middle of the berry is shown in the bottom figure. The top figure shows the THz pulse shape from four points located 2 mm from the point of the largest specular reflection. Note that the shapes of these equidistant points are similar. If the surface of the berry were flat rather than curved, the THz image would be uniformly bright and the THz pulses from points A, B, C, and D would all be the same as the specular reflection pulse. By developing a relationship between the shape of the reflected THz wave and the local inclination or tilt of the berry's surface, one should be able to determine the radius of curvature of the berry, and therefore its approximate size.

4. Application of THz Gouy Phase Shift to Crop Yield Estimation

In this section, two central issues in applying THz Gouy phase shifts to crop yield estimations are discussed: (a) why use THz imaging rather than visible

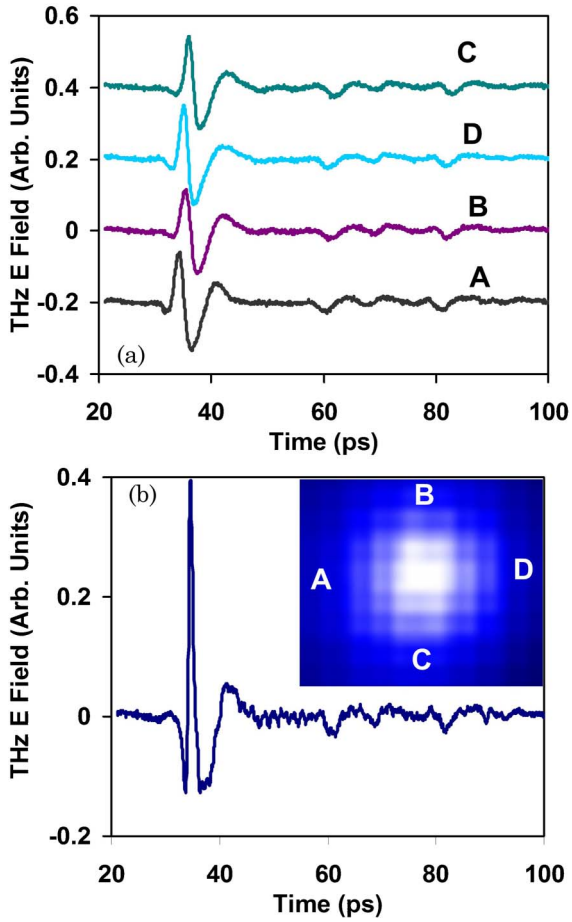

Fig. 6. (Color online) Change of THz pulse shape with the local curvature of the grape's surface. The bottom plot shows the reflected THz pulse from the specular reflection from brightest part of the THz image (bottom inset). The top curves show the reflected THz pulses from positions A, B, C, and D, which are all 2 mm from the position of the brightest specular reflection. Note that the shapes of pulses A, B, C, and D are similar to each other but different from the specularly reflected pulse.

light imaging? and (b) what options are available for a real-time fieldable THz imaging system?

A. THz Versus Visible Light Imaging

Remote sensing utilizing satellite or airborne imaging in several spectral bands has been applied to agriculture monitoring. Typically by examining the difference in light reflection at two or more visible or near-infrared spectral bands, estimations of foliage health can be used to estimate the crop yield. For example, the Normalized Difference Vegetation Index uses spectral data from 580–680 nm (corresponding to absorption from chlorophyll) and 725–1100 nm (corresponding to high reflectance from the leaf structure) to create images of plant growth, vegetation cover, and biomass production. In the case of crop estimation in vineyards, there is not a good correlation between multispectral satellite imaging and the crop yield; grape vines may be pruned several times in a growing season so that there is no strict correlation between the "greenness" of the foliage or canopy size and yield. Moreover, since the grape clusters are typically partially covered by the canopy, direct visible imaging of the grape berries is difficult.

The current practice for estimating grapevine yield involves the random selection of a few vines within a vineyard and manually counting the clusters. Even if one considers increasing the speed of counting by visible imaging using cameras in the vineyard, the canopy must be first removed prior to acquiring visible images. The potential advantage of THz versus visible imaging is the ability of THz radiation to penetrate through a thin canopy *in situ*.

Using THz imaging (or visible imaging) to count the number of berries per cluster would probably be complicated by "shadowing" effects: A berry in the foreground will hide the presence of another berry behind it. It is generally accepted that the contribution of clusters per vine, berries per cluster, and berry weight to the final yield are approximately 60%, 30%, and 10%, respectively. It is difficult to accurately estimate a major contributor (60%) to the final yield since the number of vines selected for manual counting is typically less than 1%. Even if shadowing makes the estimation of the number of berries per cluster difficult, THz imaging still can be used to measure the number of clusters per vine and berry weight, which collectively determine 70% of the crop yield estimate.

B. Prospects for Real-Time THz Imaging

The pixel-by-pixel imaging experiments described in Sections 2 and 3 are clearly too slow to be practical. Roughly 1 h is required to acquire the images with our current system. However, various real-time THz imaging systems have been demonstrated or are under development that might enable the images to be acquired in real time and on site. If a real-time imaging system were feasible, one would be able to sample a much larger fraction of the vines than could possibly be manually counted.

The THz imaging methods have been rapidly developing over the past 10 years [1]. Real-time THz imaging, in particular for concealed weapons and explosives detection, has been a very active area of development [4,5]. However, these systems are only beginning to be field tested. Since video-rate millimeter wave (MMW) imaging systems are more technically advanced than their THz counterparts, a near-term possibility for a fieldable system might be a video-rate active MMW imaging system. Numerous MMW systems have been developed and deployed for video-rate imaging of concealed weapons [17,18]. While these systems are below the THz frequency range, the upper limit (~94 GHz) borders the lower bound of the THz frequency range (100 GHz). Since the Gouy phase shift [Eq. (6)] for a 94 GHz MMW imaging system would be $-\pi/2$ for a 1 m standoff from a grape cluster, one could imagine a pulsed MMW imaging system that operates on similar Gouy phase shift principles as described in Section 3.

5. Conclusion

THz imaging can be used to differentiate grape berries from the leaves and stems. Berries can be differentiated using a THz Gouy phase shift in the reflected THz waveform. The Gouy phase shift arises due to the defocusing of the THz reflected beam on the receiver due to a strong curvature of the fruit's surface. The differentiation occurs soon after the grape berries appear in early June and continues through harvest.

Since THz wave imaging can be used to differentiate berries from the stems and leaves of a vineyard, a natural question is to what extent this is generally applicable to estimation of yields of other crops. Our preliminary work on imaging of other common thin-skinned, high-water-content crops such cherries, blueberries, and plums shows that the THz imaging method can be used to differentiate these fruits from the leaves and stems as well. Moreover, by adjusting the focal distance from the THz lenses to the fruit in Eq. (6), it should be possible to design the THz optical components for a workable standoff distance. In the case of vineyards, a 1 m distance is reasonable. By imaging high-water-content fruits from through a thin canopy, THz imaging may prove to be a useful method of crop estimation when either pruning techniques or canopy's presence interferes with alternative crop estimation methods.

Helpful discussions with J. M. Joseph are gratefully acknowledged.

References

1. D. Mittleman, "Terahertz imaging," in *Sensing with Terahertz Radiation*, D. Mittleman, ed. (Springer, 2003), pp. 117–149.
2. *Terahertz Sensing Technology Volume 2: Emerging Scientific Applications & Novel Device Concepts*, D. L. Woolard, W. R. Loerop, and M. S. Shur, eds. (World Scientific, 2003).
3. C. J. Strachan, T. Rades, D. A. Newnham, K. C. Gordon, M. Pepper, and P. F. Taday, "Using terahertz pulsed spectroscopy to study crystallinity of pharmaceutical materials," Chem. Phys. Lett. **390**, 20–24 (2004).
4. J. F. Federici, B. Schulkin, F. Huang, D. Gary, R. Barat, F. Oliveira, and D. Zimdars, "THz imaging and sensing for security applications—explosives, weapons, and drugs," Semicond. Sci. Technol. **20**, S266–S280 (2005).
5. J. F. Federici, D. Gary, R. Barat, and Z.-H. Michalopoulou, "Detection of explosives by terahertz imaging," in *Counter-Terrorism Detection Techniques of Explosives*, J. Yinon, ed. (Elsevier, 2007), p. 323.
6. Z.-K. Yan, H.-J Zhang, and Y.-B. Ying, "Research progress of terahertz wave technology in quality measurement of food and agricultural products," Spectrosc. Spectral Anal. (Beijing) **27**, 2228–2234 (2007).
7. S. Hadjiloucas, L. S. Karatzas, and J. W. Bowen, "Measurements of leaf water content using terahertz radiation," IEEE Trans. Microwave Theory Tech. **47**, 142–149 (1999)
8. S. Hadjiloucas, R. K. H. Galvao, and J. W. J. Bowen, "Analysis of spectroscopic measurements of leaf water content at terahertz frequencies using linear transforms," J. Opt. Soc. Am. A **19**, 2495–2509 (2002).
9. M. Koch, S. Hunsche, P. Schuacher, M. C. Nuss, J. Feldmann, and J. Fromm, "THz-imaging: A new method for density mapping of wood," Wood Sci. Technol. **32**, 421–427 (1998).
10. M. Reid and R. Fedosejevs, "Terahertz birefringence and attenuation properties of wood and paper," Appl. Opt. **45**, 2766–2772 (2006).
11. H. S. Chua, P. C. Upadhya, A. D. Haigh, J. Obradovic, A. A. P. Gibson, and E. H. Linfield, "Terahertz time-domain spectroscopy of wheat grain," in *Conference Digest of the 2004 Joint 29th International Conference on Infrared and Millimeter Waves and 12th International Conference on Terahertz Electronics* (IEEE, 2004), pp 399–400.
12. H. S. Chua, J. Obradovic, A. D. Haigh, P. C. Upadhya, O. Hirsch, D. Crawley, A. A. P. Gibson, and E. H. Linfield, "Terahertz time-domain spectroscopy of crushed wheat grain," in *2005 IEEE MTT-S International Microwave Symposium* (IEEE, 2005), p 4.
13. Y. L. Hor, J. F. Federici, and R. L. Wample, "Nondestructive evaluation of cork enclosures using terahertz/millimeter wave spectroscopy and imaging," Appl. Opt. **47**, 72–78 (2008).
14. S. E. Siegman, *Lasers* (University Science Books, 1986).
15. A. B. Ruffin, J. V. Rudd, J. F. Whitaker, S. Feng, and H. G. Winful, "Direct observation of the Gouy phase shift with single-cycle terahertz pulses," Phys. Rev. Lett. **83**, 3410–3413 (1999).
16. G. S. Howell, C. Schutte, and J. Treloar, "Crop estimation and sampling to achieve optimal fruit maturity and quality under michigan condition," Final Report to the Michigan Grape and Wine Industry Council, Research and Education Advisory Committee, 2006.
17. See, for example, D. M. Sheen, D. L. McMakin, and T. E. Hall, "Detection of explosives by millimeter-wave imaging," in *Counter-Terrorism Detection Techniques of Explosives*, J. Yinon, ed. (Elsevier, 2007), p. 237.
18. R. Doyle, B. Lyons, A. Lettington, T. McEnroe, J. Walsh, J. McNaboe, P. Curtin, and S. Bleszynski, "Stand-off detection of hidden threat objects on personnel at checkpoints and in public areas using active millimetre-wave imaging," Proc. SPIE **5619**, 90–97 (2004).